# High Thermoelectric Performance in PbSe–$NaSbSe_2$ Alloys from Valence Band Convergence and Low Thermal Conductivity

*Tyler J. Slade, Trevor P. Bailey, Jann A. Grovogui, Xia Hua, Xiaomi Zhang, Jimmy Jiahong Kuo, Ido Hadar, G. Jeffrey Snyder, Chris Wolverton, Vinayak P. Dravid, Ctirad Uher, and Mercouri G. Kanatzidis**

**PbSe is an attractive thermoelectric material due to its favorable electronic structure, high melting point, and lower cost compared to PbTe. Herein, the hitherto unexplored alloys of PbSe with $NaSbSe_2$ ($NaPb_mSbSe_{m+2}$) are described and the most promising p-type PbSe-based thermoelectrics are found among them. Surprisingly, it is observed that below 500 K, $NaPb_mSbSe_{m+2}$ exhibits unorthodox semiconducting-like electrical conductivity, despite possessing degenerate carrier densities of ≈$10^{20}$ $cm^{-3}$. It is shown that the peculiar behavior derives from carrier scattering by the grain boundaries. It is further demonstrated that the high solubility of $NaSbSe_2$ in PbSe augments both the thermoelectric properties while maintaining a rock salt structure. Namely, density functional theory calculations and photoemission spectroscopy demonstrate that introduction of $NaSbSe_2$ lowers the energy separation between the L- and Σ-valence bands and enhances the power factors under 700 K. The crystallographic disorder of $Na^+$, $Pb^{2+}$, and $Sb^{3+}$ moreover provides exceptionally strong point defect phonon scattering yielding low lattice thermal conductivities of 1–0.55 W $m^{-1}$ $K^{-1}$ between 400 and 873 K without nanostructures. As a consequence, $NaPb_{10}SbSe_{12}$ achieves maximum $ZT$ ≈1.4 near 900 K when optimally doped. More importantly, $NaPb_{10}SbSe_{12}$ maintains high $ZT$ across a broad temperature range, giving an estimated record $ZT_{avg}$ of ≈0.64 between 400 and 873 K, a significant improvement over existing p-type PbSe thermoelectrics.**

## 1. Introduction

Thermoelectric modules allow for interconversion between heat and electrical energy and are attractive for emerging applications in clean energy generation and solid-state cooling.[1,2] Unfortunately, the high cost and relatively low conversion efficiencies of even high quality thermoelectric materials currently restrict usage to small scale and niche applications, making further advancement necessary to achieve widespread commercialization.[3] The key challenge in developing efficient thermoelectrics is the realization of materials that together possess high electrical conductivity, $\sigma$, large Seebeck coefficient, $S$, and low thermal conductivity, $\kappa_{tot}$, as parameterized in the dimensionless figure of merit $ZT = \frac{\sigma S^2}{\kappa_{tot}} T$ in which $T$ is the absolute temperature.[4,5] Unfortunately, attaining substantial $ZT$ values has proven to be an extremely difficult task, as the thermoelectric properties $\sigma$, $S$, and $\kappa$ are intimately coupled through both the electronic structure and charge carrier density such that optimization of any one property generally degrades another and makes the development of robust strategies to enhance $ZT$ very elusive.[6,7]

Lead chalcogenides are among the premier materials for intermediate temperature (cold and hot sides, respectively, in the range 400–900 K) heat to electrical energy conversion, as a number of powerful routes to independently engineer the electronic and thermal properties have been developed,[8–13] culminating in outstanding maximum $ZT$ greater than 2 at 923 K in Na-doped PbTe–SrTe.[14,15] In contrast, the top PbSe-based alloys significantly underperform compared to PbTe, with maximum $ZT$s ≈1.6 near 923 K.[16–18] Despite possessing inferior figures of merit, PbSe remains an attractive alternative because of its lower cost, intrinsically lower lattice thermal conductivity,[19] superior mechanical robustness, and higher maximum operating temperature.[20] As such, PbSe continues to garner significant attention directed toward improving its thermoelectric performance.

T. J. Slade, Dr. I. Hadar, Prof. M. G. Kanatzidis
Department of Chemistry
Northwestern University
Evanston, IL 60208, USA
E-mail: m-kanatzidis@northwestern.edu

T. P. Bailey, Prof. C. Uher
Department of Physics
University of Michigan
Ann Arbor, MI 48109, USA

J. A. Grovogui, X. Hua, X. Zhang, J. J. Kuo, Prof. G. J. Snyder, Prof. C. Wolverton, Prof. V. P. Dravid
Department of Materials Science and Engineering
Northwestern University
Evanston, IL 60208, USA

The ORCID identification number(s) for the author(s) of this article can be found under https://doi.org/10.1002/aenm.201901377.

DOI: 10.1002/aenm.201901377

 

Intriguingly, although the valence band structure of PbSe is more favorable than that of the conduction band for achieving high power factor ($S^2\sigma$), both p- and n-type alloys have been reported to exhibit comparable maximum figures of merit near 1.6. Furthermore, the $ZT$s of the n-type materials actually exceed those of the p-type at most temperatures,[21–25] yielding superior average $ZT$s of 1 over 300–900 K compared to values of only ≈0.5 for the p-type compounds. This is the opposite of what is observed in PbTe systems. A principal reason for this discrepancy is that while high $ZT$ in p-type PbSe is generally achieved by means of electronic band structure engineering,[16,17] which primarily improves the performance only at elevated temperatures, exceptionally low lattice thermal conductivity has been achieved in the n-type materials over a broad range of temperatures, providing a wider interval of enhancement to the figure of merit.[21,24–26] Therefore, improving the thermoelectric performance of p-type PbSe requires the integration of valence band convergence and a wide interval of ultralow thermal conductivity.

Alloys of PbSe with $NaSbSe_2$ (represented here as $NaPb_mSbSe_{m+2}$ or equivalently $NaSbSe_2$ + $m$PbSe) are a new family of materials that may be well suited to fit this need. $NaPb_mSbSe_{m+2}$ compounds can be envisioned as solid solutions between $NaSbSe_2$ and PbSe, in which the three cations are randomly distributed across the Pb sites in the $Fm\bar{3}m$ crystal structure. Because of the heavy cation disorder, all PbQ–$NaSbQ_2$ (Q = Te, Se, S) compounds are intuitively expected to exhibit strong point defect phonon scattering and low thermal conductivity. Indeed, alloys of PbTe with $ASbTe_2$ (A = Ag, Na, K) are already well-established thermoelectric materials that possess high maximum $ZT$s of 1.5–1.7 near 700 K as a consequence of their ultralow lattice thermal conductivities.[27–30] Historically, while the tellurides $AgPb_mSbTe_{m+2}$ and $NaPb_mSbTe_{m+2}$ have been well studied and proven to be outstanding thermoelectrics, the selenide and sulfide analogues have not been investigated and are strong candidates for new research.

We find that alloying $NaSbSe_2$ into PbSe has two beneficial effects on the thermoelectric properties: 1) reduction of the energy separation between L- and Σ-valence bands raises the density of states effective mass and boosts the power factors; 2) strong point-defect phonon scattering yields exceptionally low thermal conductivity without nanostructuring. As a result, properly doped $NaPb_mSbSe_{m+2}$ achieves maximum $ZT$ of 1.4 near 900 K and critically, a record estimated $ZT_{avg}$ for p-type PbSe of 0.64 over 400–873 K, marking a significant improvement on existing tellurium free p-type PbSe-based thermoelectrics. In addition, we surprisingly discovered that even when possessing degenerate carrier densities over $10^{20}$ $cm^{-3}$, the heavily doped samples of $NaPb_mSbSe_{m+2}$ compounds exhibit unusual semiconducting behavior with thermally activated electrical conductivity up to 500 K. We suggest that the unorthodox electrical transport under 500 K is the result of charge carrier scattering by the grain boundaries analogous to the behavior recently observed in $Mg_3Sb_2$ thermoelectrics.[31–33] Elimination of this effect may represent a future path toward further improving the thermoelectric performance of $NaPb_mSbSe_{m+2}$.

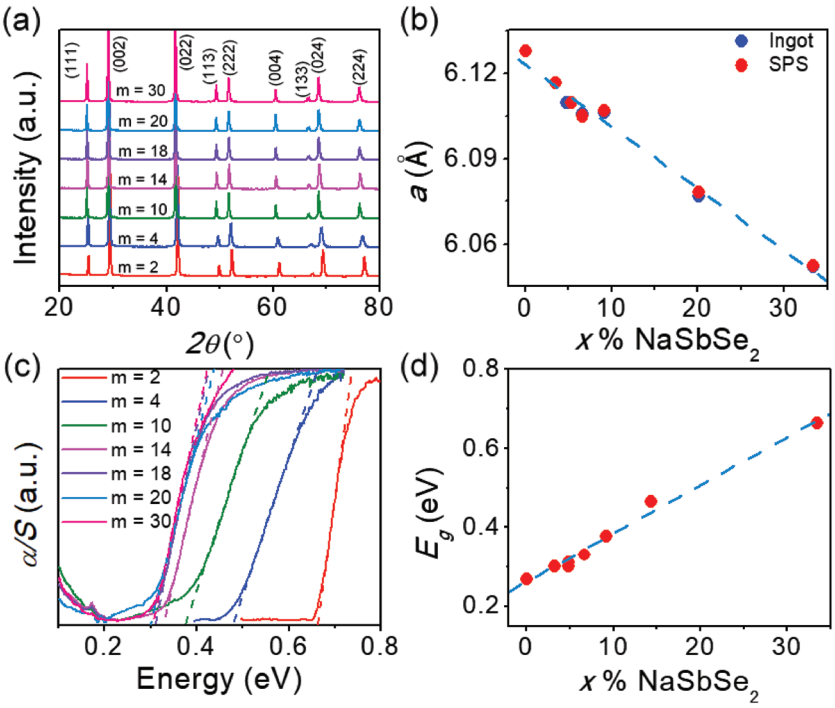


**Figure 1.** a) Powder X-ray diffraction patterns for $NaPb_mSbSe_{m+2}$ ($m$ = 2–30). b) Refined lattice parameters for $NaPb_mSbSe_{m+2}$, represented as PbSe + $x$% $NaSbSe_2$. c) Fourier transformed infrared spectroscopy spectra for the same $NaPb_mSbSe_{m+2}$ compounds (the dashed lines show the extrapolation used to estimate the bandgaps) and d) the estimated bandgaps. The dashed blue lines in (b) and (d) are guides to the eye showing the approximately linear trends in lattice parameter and bandgap as functions of $NaSbSe_2$ content. Unless noted, the data shown above was obtained from samples after SPS sintering.

## 2. Results and Discussion

### 2.1. Structural and Optical Characterization

While Na and Sb individually have limited solubility (under 2%) in lead chalcogenides,[24,34] joint integration of both $Na^+$ and $Sb^{3+}$ in equal quantities mimics the $Pb^{2+}$ and allows for dramatically higher solubility. In fact, previous work on $NaSbTe_2$–PbTe demonstrated that with proper processing, single phase samples can be prepared with even up to 50% $NaSbTe_2$.[30] Such high solubility allows access to a broad compositional space over which to study and optimize the thermoelectric properties.

To explore the solubility of $NaSbSe_2$ in PbSe, we began by synthesizing a range of $NaPb_mSbSe_{m+2}$ compounds with $m$ = 2–30 (or equivalently ≈3–33% $NaSbSe_2$). The powder X-ray diffraction (PXRD) patterns are shown in **Figure 1**a. The experimental diffraction patterns reveal no evidence of secondary

phases and are in excellent agreement with the expected peaks for the rocksalt crystal structure, suggesting that phase pure samples can be synthesized down to at least $m = 2$ (33% $NaSbSe_2$). The refined lattice parameters are presented in Figure 1b as functions of $NaSbSe_2$ fraction, i.e., $(PbSe)_{1-x}$–$(NaSbSe_2)_x$ and decrease linearly as $x$ increases ($m$ decreases) as expected for a solid solution of $NaSbSe_2$ and PbSe. The lattice parameters and diffraction patterns are identical before and after spark plasma sintering (SPS), indicating that no chemical changes occur during sintering. Similarly, Fourier transformed infrared (FTIR) spectroscopy data and the corresponding estimated bandgaps presented respectively in Figure 1c,d show that the bandgaps increase in a linear manner from 0.27 to 0.67 eV as greater fractions of $NaSbSe_2$ are added to PbSe. This result is consistent with the wider electronic bandgap of ≈1.1 eV for $NaSbSe_2$ compared to that of 0.27 eV for PbSe. Together, the clean diffraction patterns paired with linear trends in lattice parameters and bandgaps support the notion that $NaSbSe_2$ and PbSe form a solid solution over the compositions of interest ($m = 2$–30).

### 2.2. Microstructural Characterization of $NaPb_mSbSe_{m+2}$

To characterize the microscopic nature of the PbSe–$NaSbSe_2$ alloys, we performed a combination of transmission electron microscopy (TEM) and scanning electron microcopy (SEM). A characteristic high-resolution TEM image of a $m = 10$ sample is presented in **Figure 2**a and shows no evidence of nanoscale precipitation. The selected area electron diffraction pattern shown in Figure 2b is in good agreement with the expected rock-salt structure and exhibits no unexpected diffraction spots, further indicating a phase pure material. Considering that the closely related PbSe–$AgSbSe_2$ ($AgPb_mSbSe_{m+2}$) alloys have been reported to be heavily nanostructured,[35] these findings may initially be surprising. Despite this, the TEM results reported here are consistent with our previous work on the telluride analogues, $NaPb_mSbTe_{m+2}$, which were also found to be free of nanostructures after SPS sintering.[30] The lack of nanostructures in $NaPb_mSbSe_{m+2}$ is moreover in agreement with theoretical calculations on phase stability in these systems, which find lower mixing energies for PbQ–$NaSbQ_2$ alloys than for PbQ–$AgSbQ_2$,[30,36,37] suggesting that mixtures of lead chalcogenides with $NaSbQ_2$ are less prone to the formation of nanoprecipitates than those alloyed with $AgSbQ_2$.

Intriguingly, while the TEM analysis shows the PbSe–$NaSbSe_2$ alloys to be single phase on the nanoscale, the SEM results shown in Figure 2c–g indicate elemental segregation at the micrometer level. Figure 2c displays a typical backscattered electron (BSE) image. Here, the image shows significant Z-contrast, suggesting that the sample is not perfectly homogeneous. Indeed, the energy dispersive spectroscopy (EDS) maps of each element (Figure 2d–g) confirm that the brighter regions in Figure 2c are richer in Pb, while the darker areas contain more Na and Sb. Considering that the powder diffraction patterns do not show evidence of secondary phases, the degree of inhomogeneity is likely small. Therefore, the data presented in Figure 2c–g likely represents

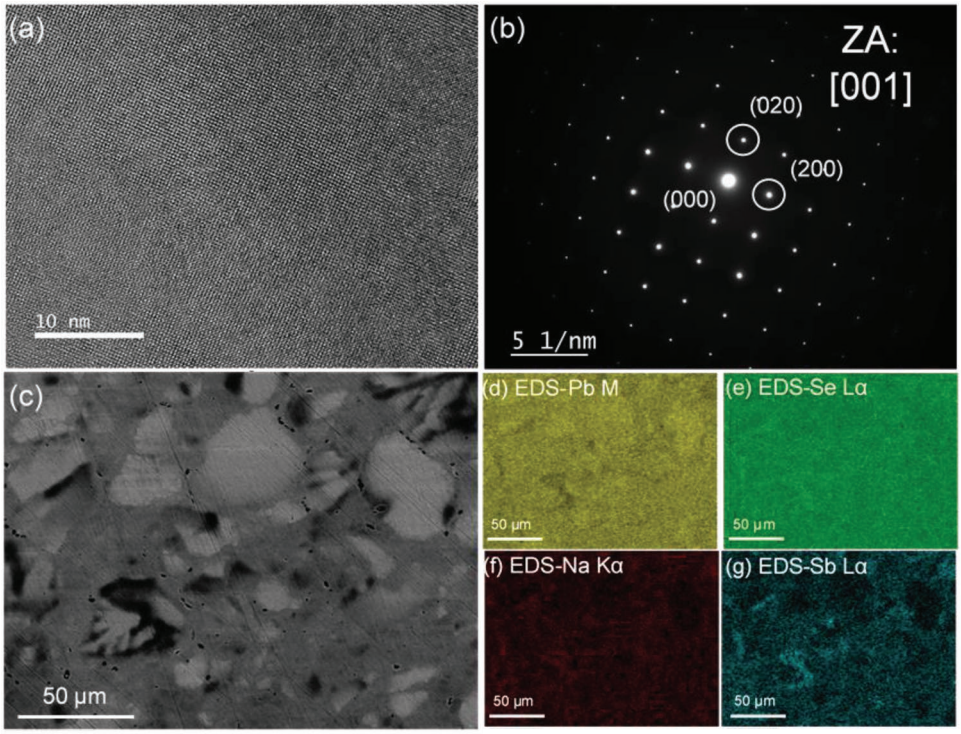


**Figure 2.** a) A characteristic high-resolution TEM image of a sample with nominal composition $Na_{1.15}Pb_{9.85}SbSe_{12}$ and b) a selected area electron diffraction pattern, both confirming a clean rocksalt structure with no nanoscale precipitates. c) Backscattered electron image showing noticeable micrometer-level Z-contrast, and d–g) EDS elemental maps over the region shown in (c). The EDS maps confirm minor elemental segregation into Pb-rich regions and Na/Sb-rich regions.

minor perturbations of the nominal $NaPb_{10}SbSe_{12}$ stoichiometry, i.e., some regions of slightly lower $m$ (richer in $NaSbSe_2$) and other areas of slightly higher $m$ (richer in PbSe). Similar micrometer-level inhomogeneity has also been reported in as-cast ingots of the related compounds $AgPb_mSbTe_{m+2}$[38] and $NaPb_mSbTe_{m+2}$.[30] Considering the thermoelectric properties of identically prepared samples are consistent (Figure S10, Supporting Information), it is unlikely that the above inhomogeneity has a significant impact on the thermoelectric properties.

### 2.3. Thermoelectric Properties of p-Type $NaPb_mSbSe_{m+2}$

Stoichiometric $NaPb_mSbSe_{m+2}$ compounds are valence-precise materials composed of $Na^+$, $Pb^{2+}$, $Sb^{3+}$, and $Se^{2-}$ ions, and therefore, are expected to be intrinsic semiconductors with low carrier densities. In principle, $NaPb_mSbSe_{m+2}$ should be tunable as n- or p-type with the proper dopants. Considering PbSe has a favorable valence-band structure for achieving high power factor, we chose to first investigate p-type $NaPb_mSbSe_{m+2}$. In previous studies on the telluride analogues, $NaPb_mSbTe_{m+2}$, the highest $ZT$s were found near the PbTe-rich side of the system ($m > 8$),[28,30] and here we focused our work on $NaPb_{10}SbSe_{12}$ ($m = 10$). To add p-type charge carriers (holes), we first introduced additional $Na^+$ into the lattice in place of $Pb^{2+}$ (i.e., $Na_{1+x}Pb_{m-x}SbSe_{m+2}$). The resulting thermoelectric properties are outlined and discussed below.

**Figure 3**a,b respectively displays the electrical conductivities and Seebeck coefficients of $Na_{1+x}Pb_{10-x}SbSe_{12}$ ($x$ = 0.01–0.20). These compounds all have a fixed fraction of ≈9% $NaSbSe_2$ alloyed into PbSe ($m = 10$ in $NaPb_mSbSe_{m+2}$) and are extrinsically doped with additional Na. The electrical conductivities rise with greater Na doping (higher $x$) reaching maximum values ≈600 S cm$^{-1}$ at ≈450 K for $x = 0.20$. The Seebeck coefficients are all positive over the measured temperatures, suggestive of p-type charge transport and decrease as the doping level rises. The trends in both electrical conductivities and Seebeck coefficients indicate that the hole density is effectively raised by the Na doping. Successful doping of $NaPb_mSbSe_{m+2}$ is confirmed by the temperature-dependent Hall effect data shown in Figure 3c. Na doping significantly increases the carrier density from 1.4 × 10$^{18}$ cm$^{-3}$ for $x = 0.01$ to 1.5 × 10$^{20}$ cm$^{-3}$ for $x = 0.15$. The Hall carrier mobilities are lastly shown in Figure 3d and rapidly drop with greater Na content. Namely, at 300 K there is a large decrease in mobility between $x = 0.01$ and 0.05 from 100 to 20 cm$^2$ V$^{-1}$ s$^{-1}$ followed by a smaller decline to 10 cm$^2$ V$^{-1}$ s$^{-1}$ for $x = 0.15$. Lastly, it should be noted that the electrical conductivities are thermally activated below ≈500K (Figure 3a), which is highly anomalous and will be explained in detail at the end of the discussion section.

**Figure 4**a shows the temperature-dependent total thermal conductivities of $Na_{1+x}Pb_{10-x}SbSe_{12}$. The measured thermal conductivities are very low and decrease as functions of temperature to converge at minimum values of ≈0.8 W m$^{-1}$ K$^{-1}$ at 873 K. At room temperature, the total thermal conductivities increase with greater Na fraction because of the higher electronic conductivities, which increase the electronic contributions to the thermal conductivity $\kappa_{elec}$. Likewise, the estimated lattice thermal conductivities (shown as $\kappa_{tot} - \kappa_{elec}$) in Figure 4b are exceptionally low, with values under 1 W m$^{-1}$ K$^{-1}$ over nearly the full temperature regime, all of which mostly converge to a minimum of ≈0.55 W m$^{-1}$ K$^{-1}$ at 873 K. The $ZT$s are finally displayed in Figure 4c and increase with both temperature and doping level, achieving high maximum values of ≈1.3 at 873 K for $x = 0.20$.

To explore the best route to tune the carrier density in $NaPb_mSbSe_{m+2}$, we also attempted to introduce additional Na in place of Sb (i.e., $Na_{1+x}Pb_{10}Sb_{1-x}Se_{12}$). **Figure 5**a,b respectively displays the corresponding electrical conductivities and Seebeck coefficients. Here, the electrical conductivity increases dramatically between $x = 0.05$ and 0.10, accompanied by a decrease of the Seebeck coefficients, suggestive of an increased hole concentration. As the Na doping level is further increased from $x =$ 0.10 to 0.15, the Seebeck coefficients remain largely unchanged, indicating little effect on the carrier density. However, the electrical conductivity of the more heavily doped compound is suppressed under ≈600 K, while at high temperatures, the electrical conductivities of both compounds converge to similar values near 200 S cm$^{-1}$. The temperature-dependent charge carrier density of the $x = 0.10$ sample (shown in Figure 5c) shows a

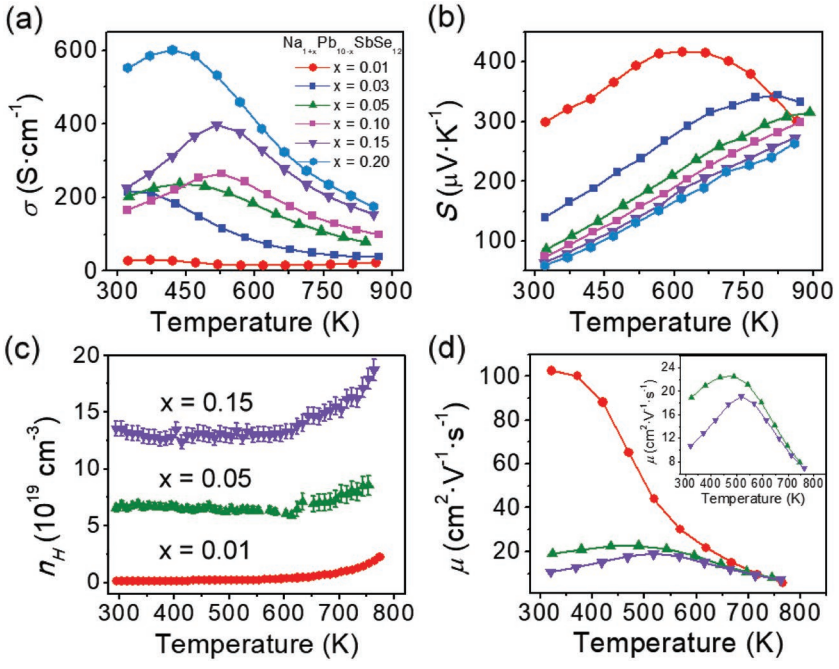


**Figure 3.** Temperature-dependent a) electrical conductivities, b) Seebeck coefficients, c) Hall carrier densities, and d) Hall carrier mobilities for $Na_{1+x}Pb_{10-x}SbSe_{12}$. The inset in (d) shows a close up of the mobilities of samples for which $x = 0.05$ and 0.15, emphasizing the positive temperature dependence of $\mu$ below 500 K.

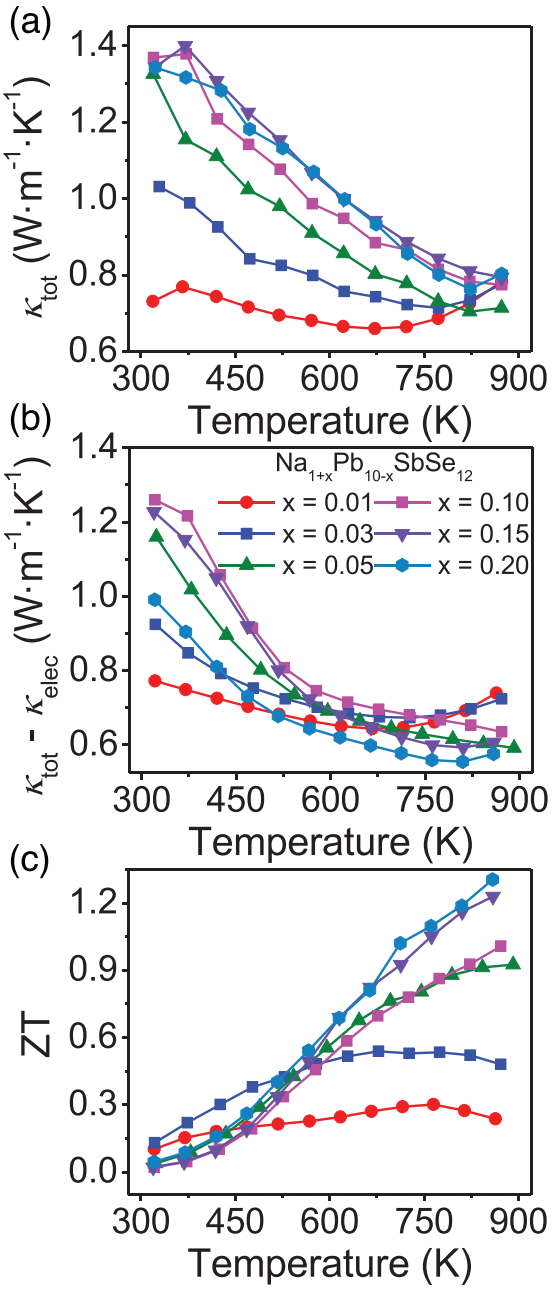


**Figure 4.** Temperature-dependent a) total thermal conductivities, b) estimated lattice thermal conductivities ($\kappa_{tot} - \kappa_{elec}$), and c) *ZT*s for $Na_{1+x}Pb_{10-x}SbSe_{12}$.

nearly constant value of $\approx 2 \times 10^{20}$ cm$^{-3}$ between room temperature and 650 K, the highest of all measured samples.

The higher carrier densities that can be achieved by substituting additional Na in place of Sb is the key difference between the data in Figure 5 and that presented in Figures 3 and 4. As a consequence, the power factors of $Na_{1+x}Pb_{10}Sb_{1-x}Se_{12}$ are slightly higher and achieve maximum values of 13–14 μW cm$^{-1}$ K$^{-2}$ between 700 and 873 K (Figure 5d). Furthermore, the total thermal conductivities of $Na_{1+x}Pb_{10}Sb_{1-x}Se_{12}$ shown in Figure 5e are again very low over the measured temperature regime with small differences between doping level. In general, the total thermal conductivities decrease with temperature from 1.6 to 0.8 W m$^{-1}$ K$^{-1}$ over 323–873 K. The *ZT*s are shown in Figure 5f and are slightly improved compared to those shown in Figure 4c for $Na_{1+x}Pb_{10-x}SbSe_{12}$, increasing with temperature over the full measurement range and approaching a maximum of 1.4 at 873 K for $x = 0.10$.

### 2.4. Low Lattice Thermal Conductivity in $NaPb_mSbSe_{m+2}$

Figures of merit approaching 1.4 near 900 K make $NaPb_mSbSe_{m+2}$ competitive with state-of-the-art p-type PbSe-based thermoelectrics such as PbSe–SrSe,[17] PbSe–CaS,[18] and PbSe–HgSe.[16] To understand the origin of the outstanding thermoelectric performance, we note that the lattice thermal conductivities displayed in Figures 4b are among the lowest measured in a PbSe-based alloy, particularly at intermediate temperatures under 700 K. Unfortunately, investigating the details and origin of the low thermal conductivity is challenging, primarily complicated by the fact that anomalous electrical conductivity described previously limits our ability to reliably estimate $\kappa_{elec}$. This issue is outlined in greater detail in the Supporting Information.

Yet, we can still glean several insights on the low thermal conductivities from other perspectives. From our TEM study, no nanostructures nor precipitates were observed in any of the $NaPb_mSbSe_{m+2}$ samples, suggesting that the bulk of the reduction in thermal conductivity stems from strong point defect phonon scattering, the result of the random occupation of $Na^+$, $Pb^{2+}$, and $Sb^{3+}$ on the cation sites. To provide evidence for this, we estimated the lattice thermal conductivities of undoped $NaPb_mSbSe_{m+2}$ ($m$ = 2–30) and pure PbSe and compared the experimental values with calculations from a simplified Debye–Callaway model that considered only phonon–phonon and point defect scattering.[34,39] Here, the low carrier densities of the undoped samples yield small $\kappa_{elec}$, making any errors in the estimated $\kappa_{lat}$ stemming from the unusual electrical conductivity negligible. Details concerning the model can be found in the Supporting Information. The data is presented in Figure S1 in the Supporting Information and shows that the $\kappa_{lat}$ of the undoped samples decreases monotonically with $NaSbSe_2$ fraction, agreeing reasonably well with the projected values from the alloy model. While the strong bipolar diffusion in the undoped samples limits analysis of the temperature dependence, the results provide support that the primary origin of the extremely low lattice thermal conductivities in $NaPb_mSbSe_{m+2}$ is point defect scattering, although other mechanisms may also be at play.

### 2.5. Role of $NaSbSe_2$ in Modifying the Electronic Structure of PbSe

In addition to the low lattice thermal conductivities, the thermoelectric performance in $NaPb_mSbSe_{m+2}$ is moreover augmented by the electronic properties. Namely, the Seebeck coefficients shown in Figures 3b and 4b are comparable to those found in band engineered PbSe,[16,17] indicating $NaSbSe_2$ may have

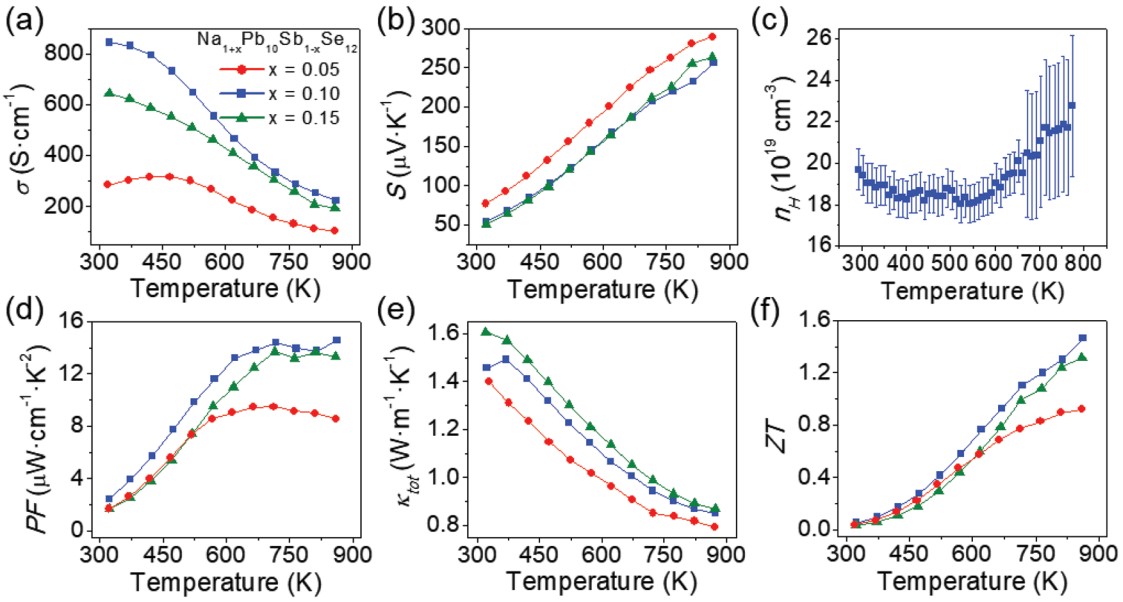


**Figure 5.** Temperature-dependent thermoelectric properties of $Na_{1+x}Pb_{10}Sb_{1-x}Se_{12}$. a) Electrical conductivity, b) Seebeck coefficient, c) Hall carrier concentration for $x = 0.10$, d) power factors, e) total thermal conductivities, and f) $ZT$.

a favorable impact on the electronic structure of PbSe. To probe this, we used density functional theory (DFT) to calculate the band structures of several PbSe–$NaSbSe_2$ compounds. The results are presented in **Figure 6**a and demonstrate that $NaPb_mSbSe_{m+2}$ retains the same general features as that of pure PbSe. In particular, the $NaPb_mSbSe_{m+2}$ compounds are direct gap semiconductors with a primary bandgap at the L-point of the Brillouin zone and secondary valence and conduction bands deeper in energy at the Σ-point. The calculations further demonstrate that the bandgap widens as a function of the $NaSbSe_2$ fraction, consistent with the experimental trends observed in Figure 1d.

Importantly, Figure 6b reveals that the energy offset between the L- and Σ-valence bands ($\Delta E_{L-\Sigma}$) significantly decreases with greater $NaSbSe_2$ content, from ≈0.3 to 0.14 eV between $n = 0$ and 2. This supports the suggestion that high Seebeck coefficients may result from the converging bands. Care must be taken in this interpretation, as the calculations also show that as more $NaSbSe_2$ is added to PbSe, both valence and conduction bands flatten, i.e., the band effective mass $m_b^*$ increases. This is understandable, as introduction of $Na^+$ and $Sb^{3+}$ into PbSe is expected to increase the ionicity of the compound and in turn widens the bandgap and flattens the bands.[40] Considering the large fraction of $NaSbSe_2$ found in $NaPb_{10}SbSe_{12}$ (≈9%), it is reasonable to expect a significantly higher $m_b^*$ for this material compared to PbSe. Unfortunately, because band flattening (increasing $m_b^*$) and band convergence (increasing $m_{DOS}^*$) will both enlarge the Seebeck coefficient ($S \propto m_{DOS}^*$ and $m_{DOS}^* = N_V^{2/3} m_b^*$, where $N_V$ is the degeneracy of the bands), these two processes must be separated to understand both the origin of the high Seebeck coefficients and the full role of $NaSbSe_2$ in PbSe.

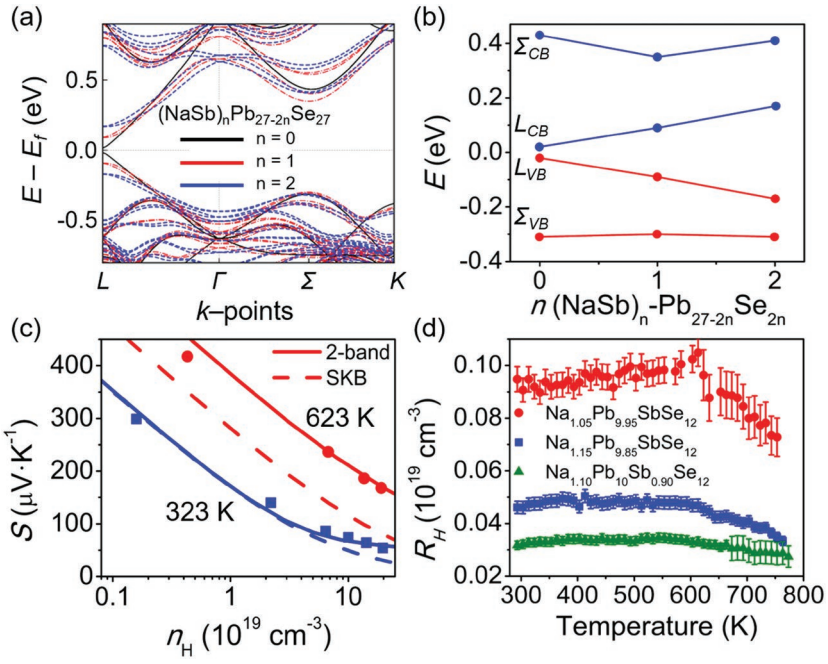


**Figure 6.** a) DFT calculated band structures for $NaPb_mSbSe_{m+2}$ (shown as $Na_nSb_nPb_{27-2n}Se$ and representing 0%, 4%, and 8% $NaSbSe_2$, respectively). b) DFT calculated energy differences between L- and Σ-bands for the band structures shown in (a). c) Pisarenko plots for $NaPb_{10}SbSe_{12}$ at 323 and 623 K. The theoretical lines were calculated with both a single-band (SKB) and two-band model, shown as dashed and solid lines, respectively. d) Temperature-dependent Hall coefficients for p-type doped $NaPb_{10}SbSe_{12}$.

To decouple the potential impacts of band flattening and valence-band convergence in $NaPb_mSbSe_{m+2}$, we generated theoretical graphs of the carrier density versus Seebeck coefficient (Pisarenko plots) using both a single Kane band (SKB model)[20,41–43] and a two-band model[43] and compared the results with the experimental data. The details of our Pisarenko calculations are shown in the Supporting Information and the results are presented in Figure 6c. The Pisarenko curves confirm the increase in effective mass predicted by the DFT calculations, as we find that an L-band density of states mass of $m_L^* = 0.37\ m_e$ is required to fit the experimental data at 323 K, a considerable increase over that of pure PbSe ($m_L^* = 0.27m_e^*$). We moreover find that while both the single-band and 2-band curves can be fit reasonably well with the experimental data at 323 K, the SKB model severely underestimates the measured points at 623 K, implying that the effective mass of $NaPb_{10}SbSe_{12}$ increases with heating faster than anticipated from a SKB model and thus suggesting the single-band model is incorrect. On the other hand, the two-band model provides a much better prediction of the experimental data at 623 K while also giving a more satisfactory fit to the high $n_H$ data at 323 K. The good agreement between the two-band Pisarenko curves and experimental data therefore supports the results observed in the calculated electronic band structures, that the energy separation between the L- and Σ-valence bands decreases upon alloying with $NaSbSe_2$ and that both bands contribute to the charge transport.

To provide further experimental support for two-band charge transport, we measured the temperature-dependent Hall coefficients, $R_H$, the results of which are shown in Figure 6d. In p-type lead chalcogenides, a peak in $R_H$ plotted as a function of temperature is often interpreted as evidence of multiband behavior, characteristic of the carriers redistributing between converging bands.[43–46] The measured Hall coefficients displayed in Figure 6d are approximately constant functions of temperature until 600 K, at which point they decrease with further heating. Close inspection of the individual curves of Figure 6d does reveal that the Hall coefficients increase weakly with temperature before ≈600 K (Figure S8, Supporting Information); however, the peaks in the $R_H$ versus $T$ plots are clearly much weaker than what is typically observed in p-type PbSe.[43] Although at first glance, the Hall data appears characteristic of single-band transport, in disagreement with the DFT calculations and Pisarenko plots, this interpretation requires closer inspection.

First, the decrease in the experimental $R_H$ values as functions of temperature beginning at 600 K cannot, as one may initially suspect, be from the onset of intrinsic conduction, as the Seebeck coefficients (shown in Figure 3b) do not exhibit a corresponding downturn. Furthermore, no evidence for bipolar diffusion is found in the estimated electronic and lattice thermal conductivities (Figure 4b; Figure S4, Supporting Information, respectively). Therefore, despite the relatively flat temperature dependence, the Hall data is likely not characteristic of single-band transport. As discussed by Allgaier, a maximum in a plot of $R_H$ versus $T$ occurs in two-band systems not when the energies of each band are equal, as is commonly suggested, but instead when the respective contributions to the total electrical conductivity from each band are equal.[47] As a result, signs of band convergence in the electronic transport may be suppressed even in true multiband systems depending on the specific parameters of each band.

Interestingly, work by Wang et al. on p-type PbSe–SrSe shows very similar Hall data for high fractions of Sr (8–12%), in which the Hall coefficients are nearly independent of temperature until ≈600–700 K,[17] providing an example of a well-established two-band system lacking a strong $R_H$ peak. This may be understood by considering Allgaier's general two-band model and the impact of $NaSbSe_2$ (and Sr) on the electronic structure. As discussed previously, introducing $NaSbSe_2$ (or Sr) into PbSe will flatten the bands, increasing $m_b^*$ and therefore lowering the mobility ratio between L- and Σ-bands. In this interpretation, the relatively flat temperature dependence of $R_H$ between 300 and 600 K suggests that both L- and Σ-bands have comparable partial electrical conductivities over this temperature range (i.e., both contribute significantly to the charge transport), and the decrease in $R_H$ beginning at 600 K marks the temperature at which the majority of the conduction occurs in the second band.[47,48]

As a final means of experimentally probing the electronic band edge positions, we utilized photoemission yield spectroscopy in air (PYSA)[49–51] to determine the work functions of several nominally undoped samples of $NaPb_mSbSe_{m+2}$ for $m$ = 10–30 and pure PbSe. The photoemission spectra are shown in **Figure 7**a. Extrapolating the linear region of each spectrum to the baseline determines the work function. Because these samples are only weakly p-type (see Figure S2 in the Supporting Information), the carrier densities are small, and the work functions give the energies of the valence band edge (L-point) versus vacuum. Adding the experimentally determined bandgaps to the work functions will therefore determine the energy of the conduction band edge. The results are displayed in Figure 7b and show that between 0% and 9% $NaSbSe_2$ the valence band edge (work function) moves deeper in energy from ≈4.97 to 5.06 eV, while the conduction band edge remains approximately unchanged.

Since the room temperature energy difference between L- and Σ-bands in pure PbSe is known to be ≈0.25 eV,[17,43] we can use the observed energy shifts in the measured work functions to estimate the energy difference between L- and Σ-valence bands. To do this, we must assume that the position of the Σ-band does not change appreciably with $NaSbSe_2$ alloying. This assumption is supported by the DFT calculated band structures shown in Figure 6a and is further justified considering the significant cation (Pb s-orbital) character of valence band at the L-point, whereas the Σ-band is expected to be mostly anion (Se p-orbital) in character and therefore weakly impacted by alloying onto the cation site.[40,52] The energy differences between L- and Σ-valence bands estimated from the work functions of each compound are presented in Figure 7c and show that the $\Delta E_{L-\Sigma}$ decreases with $NaSbSe_2$ fraction down to ≈0.16 eV for 9% $NaSbSe_2$. These results are in general agreement with the DFT calculations shown in Figure 6a (which are calculated for 0%, 4%, and 8% $NaSbSe_2$), albeit the experimental values are somewhat higher than the calculated energy differences. The experimentally estimated values of $\Delta E_{L-\Sigma}$ are moreover in excellent agreement with the theoretical 2-band Pisarenko calculations found in Figure 6c. To generate the Pisarenko curve, we used an energy difference ($\Delta E_{L-\Sigma}$) of

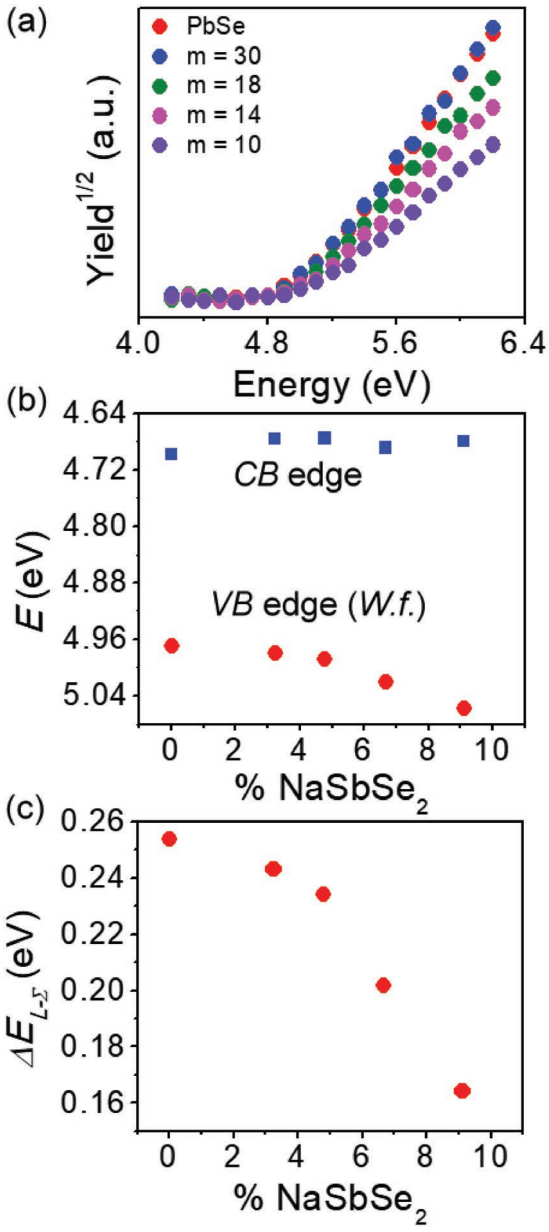


**Figure 7.** a) Photoemission yield spectroscopy in air (PYSA) spectra for nominally undoped samples of $NaPb_mSbSe_{m+2}$ ($m$ = 10–30 and pure PbSe). b) Energies of the valence band edges (work functions) and conduction band edges for each sample extracted from the linear regions of the photoemission spectra, shown as red and blue points, respectively. 9% $NaSbSe_2$ corresponds to the $m$ = 10 sample discussed most thoroughly in the text. c) Experimentally estimated energy differences between L- and Σ-valence bands for each sample.

0.15 eV at room temperature (see the Supporting Information for more details) to fit the experimental Seebeck coefficients, clearly in strong agreement with the experimental value of 0.16 eV.

The combined results from the DFT calculations, the 2-band Pisarenko curves, experimental Hall effect data, and photoemission experiments all indicate that introducing $NaSbSe_2$ into PbSe both raises the band effective mass and reduces the energy separation of the L- and Σ-valence bands, allowing both bands to contribute similarly to charge transport even at relatively low temperatures near 300 K. The net effect of the two-band transport is significantly increased valley degeneracy ($N_v$ = 4 and 12 for the L- and Σ–bands, respectively), which boosts the density of states effective mass and enhances the Seebeck coefficients as is well known in many high quality thermoelectrics.[8] Indeed, as displayed in Figure S9 in the Supporting Information, at temperatures under ≈700 K, our optimally doped $NaPb_{10}SbSe_{12}$ has superior power factors to both Na-doped PbSe and band engineered PbSe–HgSe.[16] Considering that our $NaPb_{10}SbSe_{12}$ samples have comparable carrier concentrations and lower charge carrier mobilities than the aforementioned materials, we attribute the improved power factors (under 700 K) to the fact that in $NaPb_{10}SbSe_{12}$, both valence bands contribute more significantly to the charge transport even near room temperature.

### 2.6. Thermoelectric Figure of Merit

In $NaPb_mSbSe_{m+2}$, the high solubility of $NaSbSe_2$ in PbSe allows for a significant fraction (≈9% for $m$ = 10) of $NaSbSe_2$ to be incorporated into the PbSe matrix. As a consequence, both extremely low lattice thermal conductivity and two-band charge transport are accessed over a wide temperature interval, substantially augmenting the thermoelectric performance. As an illustration, the temperature-dependent $ZT$s for optimally doped $NaPb_{10}SbSe_{12}$ with several of the highest performing p-type PbSe alloys found in the literature are presented in **Figure 8**a. While the maximum $ZT$s at high temperature are somewhat lower in $NaPb_{10}SbSe_{12}$ compared to the other materials, the $ZT$s found here are superior over nearly the full range of temperatures. The broad span of improved $ZT$ has a direct impact on the performance $NaPb_{10}SbSe_{12}$ may reach when integrated into a thermoelectric module. This is parameterized by the device figure of merit $ZT_{avg}$ (also often referred to as $ZT_{dev}$, $ZT_{effective}$, or $ZT_{eng}$ in other publications) and related to the energy conversion efficiency $\eta$ as follows[53–55]

$$\eta = \left(\frac{T_H - T_C}{T_H}\right) \cdot \frac{\sqrt{1+ZT_{avg}} - 1}{\sqrt{1+ZT_{avg}} + (T_C/T_H)} \quad (1)$$

Here, $T_H$ and $T_C$ are the hot and cold side temperatures, respectively. We utilized the method presented by Snyder and Snyder to estimate the device $ZT$ directly from the thermoelectric properties for our $NaPb_{10}SbSe_{12}$ and for the other PbSe alloys shown in Figure 8.[56] This method is considered an accurate means of estimating the device figure of merit and provides for a reliable means of comparing our $NaPb_{10}SbSe_{12}$ compounds with the state-of-the-art PbSe alloys found in the literature. Considering a cold side temperature of 400 K and hot side of 873 K, Figure 8b demonstrates that the $ZT_{avg} \approx 0.64$ of the best $NaPb_{10}SbSe_{12}$ is markedly improved compared to the competing materials and is to our knowledge the highest value yet reported in p-type PbSe. It should be pointed out that superior performance was very recently achieved in p-type Cd-alloyed $PbSe_{1-x}Te_x$;[57] however, these compounds are not tellurium

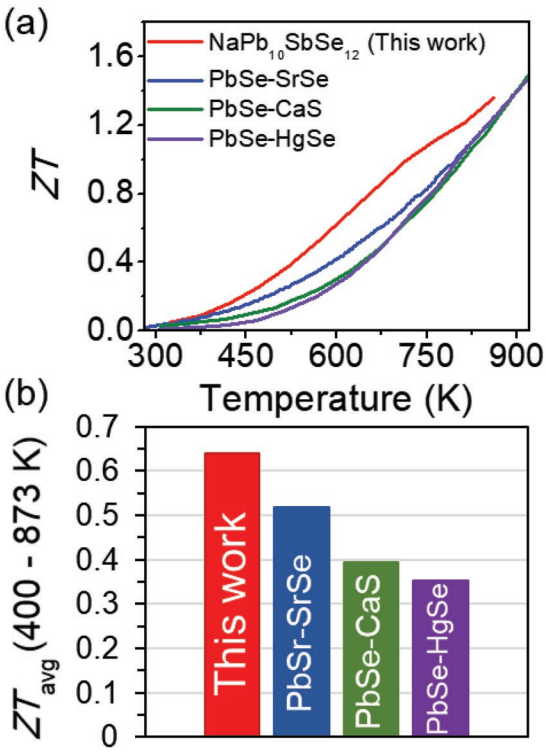


**Figure 8.** a) Traces of the temperature-dependent $ZT$ values for $Na_{1.10}Pb_{10}Sb_{0.90}Se_{12}$ (this work, denoted as $NaPb_{10}SbSe_{12}$), PbSe–SrSe,[17] PbSe–CaS,[18] and PbSe–HgSe.[16] The line for $Na_{1.10}Pb_{10}Sb_{0.90}Se_{12}$ was obtained from the averages of five separate samples (see Figure S10 in the Supporting Information). b) Comparison of the estimated $ZT_{avg}$ for the compounds shown in (a), considering cold and hot side temperatures of 400 and 873 K, respectively.

free, so this is not a direct comparison and the higher $ZT$ is expected. Evidently, $NaPb_mSbSe_{m+2}$ should have strong potential as a PbSe-based thermoelectric material for modules with intermediate operating temperature.

### 2.7. Unorthodox Charge Transport Below 500 K and Future Directions

As noted earlier, the electrical properties displayed in Figure 3 and to a lesser extent Figure 4 are highly anomalous and warrant an explanation. Namely, the Seebeck coefficients are characteristic of degenerate semiconductors and increase nearly linearly as functions of temperature between 300 and 900 K. Given the $10^{19}$–$10^{20}$ cm$^{-3}$ charge carrier concentration for the heavily doped samples, one should anticipate electrical conductivities that follow a negative temperature dependence characteristic of acoustic phonon scattering. Clearly, however, the experimental electrical conductivities shown in Figure 3a deviate dramatically from this expectation, with semiconducting-like thermally activated conduction up to ≈500 K. The Hall effect data adds to the puzzle, showing that the carrier concentrations are nearly constant over the temperatures of interest, implying the charge carrier mobilities increase with temperature under 500 K as shown in the inset of Figure 3d. This type of charge transport behavior is rarely observed in PbTe or PbSe and is therefore a highly unorthodox finding for a degenerately doped lead chalcogenide. To investigate if the unusual electrical behavior is from a phase change or temperature-dependent increase in dopant solubility, we performed in situ PXRD over 300–650 K. The variable temperature PXRD patterns shown in Figure S7 in the Supporting Information are unchanged with heating, and the corresponding lattice parameters increase linearly, indicating a different origin for the strange charge transport.

Similar results have been reported in the analogous systems $AgPb_mSbSe_{m+2}$,[58] and $AgPb_mSnSe_{m+2}$,[59] and also in SnSe-[60] and $Mg_3Sb_2$-based thermoelectrics,[31,32] all of which show thermally activated charge carrier mobilities well above room temperature. In $AgPb_mSnSe_{m+2}$ and $Mg_3Sb_2$, the atypical charge transport mechanism was first suggested to be ionized impurity scattering, which generally gives carrier mobilities with positive $T^{1.5}$ temperature dependence and was shown to be in good agreement with the experimental data for these respective compounds. Here, however, we believe that ionized impurity scattering is insufficient to explain the experimental data, namely, the Seebeck coefficients. This is best illustrated by inspecting the general equation for the Seebeck coefficient, assuming a single parabolic band, as shown below

$$S = \frac{k_B}{e}\left(\frac{(r+5/2)F_{r+3/2}(\eta)}{(r+3/2)F_{r+1/2}(\eta)} - \eta\right) \quad (2)$$

where $k_B$ is the Boltzman constant, $\eta$ is the reduced chemical potential, $F_r(n)$ are the Fermi–Dirac integrals, and $r$ is a constant that is reflective of the energy dependence of the carrier relaxation time. Because the temperature dependence of $S$ is contained in the $F_r(n)$ terms, Equation (2) clearly demonstrates that the Seebeck coefficient is a strong function of $r$. In the cases of acoustic phonon and ionized impurity carrier scattering, $r$ is equal to −1/2 and 3/2, respectively. Therefore, if the positive temperature dependence of the carrier mobilities measured in $NaPb_mSbSe_{m+2}$ is indeed due to ionized impurity scattering, $r$ would switch from 3/2 to −1/2 between 400 and 500 K when acoustic phonon scattering begins to dominate the transport. According to Equation (2), such a change in $r$ would dramatically alter the temperature dependence of the Seebeck coefficients, which is clearly not observed in Figure 3b; as such, we conclude that ionized impurity scattering is insignificant in our samples.

Recently, Kuo et al. have pointed out the same issue in their analysis of $Mg_3Sb_2$.[33] In the place of ionized impurity scattering, they proposed a model of grain boundary (GB) dominated electrical transport that provides a good theoretical prediction of both the electrical conductivities and Seebeck coefficients. In short, their model expanded on previous works, highlighting that electrostatic potential barriers can form at the grain boundaries of some polycrystalline materials, possibly originating from inhomogeneity, phase separation, lattice mismatch, defects, or impurities.[60–62] If the barrier height is sufficiently high, the charge carriers would require considerable thermal energy to pass the grain boundaries and participate in electrical conduction. Therefore, as temperature is increased, an increasing number of electrons or holes will overcome the grain boundary potentials, thereby augmenting the carrier mobility as the material is heated. At high enough

temperatures, a sufficient number of charge carriers can cross the grain boundary barriers and acoustic phonon scattering becomes the dominant mechanism, giving the classical negative temperature dependence of the carrier mobility and electrical conductivity.

The GB model is in excellent qualitative agreement with the electrical properties measured here in $NaPb_mSbSe_{m+2}$, and we believe it is the origin of the unanticipated charge transport. Because the GB scattering significantly degrades the charge carrier mobility, while providing no competing beneficial effects, it is an undesirable feature in thermoelectric materials and should be eliminated if possible. Therefore, this indicates that $NaPb_mSbSe_{m+2}$ likely has room for further improvement, as the GB scattering is severely detrimental to the power factor at lower temperatures.[33] Future work dedicated to the understanding and mitigation of this undesired effect will be thus expected to provide an additional boost to the thermoelectric performance.

## 3. Summary and Conclusions

$NaPb_mSbSe_{m+2}$ (PbSe–$NaSbSe_2$) compounds were synthesized over the range $m$ = 2–30 (3–33% $NaSbSe_2$), and the thermoelectric properties were investigated with a focus on $m$ = 10. We show that the high solubility of $NaSbSe_2$ in PbSe facilitates two beneficial effects on the thermoelectric properties. The $NaSbSe_2$ both flattens the bands and lowers the energy separation between L- and Σ-valence bands, allowing both bands to contribute to the transport even near room temperature and resulting in high power factors of ≈2–13 μW cm$^{-1}$ K$^{-2}$ in the intermediate temperature interval of 323 and 700 K. Additionally, strong point defect phonon scattering from the crystallographic disorder of $Na^+$, $Pb^{2+}$, and $Sb^{3+}$ results in exceptionally low lattice thermal conductivities of ≈1–0.55 W m$^{-1}$ K$^{-1}$ over 400–873 K without nanostructuring. Together, the high Seebeck coefficients and broad interval of low lattice thermal conductivity produce maximum $ZT$s approaching 1.4 at 873 K and outstanding $ZT_{avg}$ of 0.64 between 400 and 873 K, marking nearly a 20% improvement over existing tellurium free PbSe-based thermoelectric materials. We moreover find that $NaPb_mSbSe_{m+2}$ exhibits highly unusual semiconducting charge transport below ≈500 K, which we ascribe to charge carrier scattering at the grain boundaries. Because the GB scattering degrades the power factor at low temperatures under 500 K, future enhancement to the thermoelectric performance can likely be expected through engineering the grains in order to eliminate the undesired scattering.

## 4. Experimental Section

*Synthesis and Processing*: The starting materials were as follows: Pb wire (99.99%, American Elements, USA), Se shot (99.99%, American Elements, USA), Sb shot (99.999%, American Elements, USA), and Na cubes (99.95%, Sigma-Aldrich). Prior to synthesis, a razor blade was used to scrape the surface oxidation off the lead and sodium pieces. All sodium were handled in a $N_2$ filled glovebox.

Polycrystalline ingots with nominal compositions of $NaPb_mSbSe_{m+2}$, $Na_{1+x}Pb_{10-x}SbSe_{12}$, and $Na_{1+x}Pb_{10}Sb_{1-x}Se_{12}$ were synthesized by weighing stoichiometric quantities of each element (15 g total for each sample) into 13 mm diameter carbon-coated fused silica tubes that were then flame sealed at ≈$2 \times 10^{-3}$ Torr. The tubes were heated in a box furnace to 773 K over 12 h, held for 2 h, and then heated to 1473 K over 7 h where they were held for 5 h. The tubes were next quenched in ice water followed by annealing at 773 K for 12 h. After annealing, the tubes were again quenched in water, and the ingots were removed and ground to a fine powder with a mortar and pestle. To provide a homogeneous powder, the powders were passed through a 53 μm mesh sieve, then loaded into 12.7 mm graphite dies, and sintered into dense pellets by spark plasma sintering (SPS-211LX, Fuji Electronic Industrial Co. Ltd.) at 823 K and 40 MPa for 10 min. The pellets were finally cut and polished into bars and squares of approximate dimensions $3 \times 3 \times 10$ and $6 \times 6 \times 2$ mm$^3$ for electrical and thermal characterization, respectively. The cuts were made such that transport measurements were conducted perpendicular to the pressing direction in the SPS.

*Thermoelectric Measurements*: Using the $3 \times 3 \times 10$ mm$^3$ bars, the Seebeck coefficients and electrical conductivities were measured jointly between room temperature and 873 K using an Ulvac Riko ZEM-3 instrument operating with partial He backpressure. To limit outgassing at elevated temperatures, the bars were spray-coated with boron nitride aerosol prior to measurements except at the points needed for contacts with the electrodes and thermocouples. The uncertainty in the electrical measurements was ≈5%, which is well accepted for ZEM-3 instruments.[63] All samples showed hysteresis between the initial heating and cooling profile; however, because the properties generally stabilized upon cooling and became reversible upon further heating/cooling cycles, the data reported in this work is from the cooling profile (see Figure S11 in the Supporting Information for more details).

The thermal diffusivities ($D$) were measured with the laser flash method using the $6 \times 6 \times 2$ mm$^3$ squares in a Netzsch LFA-457 instrument, and the data were analyzed using a Cowen model with pulse correction. Before each measurement, the samples were spray-coated with a thin graphite layer to prevent errors from emissivity. The total thermal conductivities were obtained from the relation $\kappa_{tot} = DC_pd$, in which $C_p$ is the constant pressure heat capacity and $d$ is the density. The densities were calculated using the sample masses and geometries, and $C_p$ was estimated from the relationship $C_p/k_b$ (per atom) = $3.07 + 4.7 \times 10^{-4}(T - 300)$.[64] This equation had an estimated uncertainty of ≈2% across the measured temperature range. To ensure consistency with the electrical properties, the thermal data reported in this work were also obtained from the cooling cycle. The uncertainty in the total thermal conductivity arising from the measurements and calculations of the density, heat capacity, and diffusivity was estimated to be ≈8%.[63]

*Hall Effect*: The Hall effect measurements were completed using an AC 4-probe method in a homemade system with excitation fields of ±0.5 Tesla. The system uses an air-bore, helium-cooled superconducting magnet to generate the field within a high temperature oven that surrounds the Ar-filled sample probe. The carrier density $n_H$ was calculated from the Hall coefficient assuming a single carrier band, i.e., $n_H = 1/eR_H$, where $R_H$ is the Hall coefficient. The estimated error was based on the standard deviation of several data points at a single temperature.

*Microscopy Characterization*: To prepare for analysis with scanning electron microscopy-energy dispersive spectroscopy (SEM-EDS), bulk samples were ground and polished to remove maximum surface deformation and reveal the true pristine sample structure. The samples were first ground using SiC grinding paper of grit sizes 600, 800, and 1200 for 5 min each to produce an even surface with minimal roughness. Ethanol was used as the water-free lubricant, as the samples contained Na. Next, the samples were polished using a polishing pad and water-free diamond slurry of particle size 1 and 0.1 μm for 15 and 30 min, respectively. Finally, the sample was placed in a vibratory polisher with 0.05 μm alumina for 3 h to achieve the final surface finish. SEM analysis was performed at 30 kV using a Hitachi S-3400N-II SEM.

S/TEM samples were polished on one surface in the same manner as the SEM samples, with the exception of the vibratory polishing step. Once the top surface was polished, a TEM grid was fastened to the polished surface using M-bond. The sample was then thinned using

600 and 800 grit SiC grinding paper until it was less than 80 µm thick (again using ethanol as the water-free lubricant). Next, the sample was dimpled, and subsequently thinned with an argon ion mill at cryogenic temperatures. Milling took place at 2.8 kV and 8° until a hole was formed in the sample, forming an electron transparent wedge at the edge of the hole. Final milling took place at 1.5 kV and 6°, and 0.3 kV at 4° for 90 min each to properly clean the sample surface and remove any sample defects potentially introduced by higher energy ion milling. High-resolution TEM was performed at 300 kV using a JEOL ARM300F GrandARM TEM.

*Photoemission Spectroscopy*: The work functions (valence band maxima) were measured by photoemission yield spectroscopy in air (AC-2, Riken-Keiki). In PYSA, the sample is scanned by tunable monochromatic ultraviolet light (UV, 4.2–6.2 eV) under ambient conditions, and the number of generated photoelectrons is measured at each excitation energy. Photoelectrons are only generated when the photon energy is higher than the work function. The work function is determined by finding the onset of the PYSA spectra.

*Electronic Structure Calculations*: Density functional theory[65,66] calculations were performed using the Vienna ab initio Simulation Package (VASP)[67–69] with projector augmented (PAW)[70] pseudopotentials utilizing Perdew–Burke–Ernzerhof (PBE) generalized gradient approximation (GGA) exchange correlation.[71] NaSb-doped PbSe calculations were performed on 54-atom supercells created by Pb atoms with Na and Sb. The energies of Na and Sb placed far from or near each other in the PbSe lattice were calculated and those with lower energies were selected. For Pb and Na atoms, the semicore d and p electrons were treated as valence states, respectively. Both relaxation calculations and band structure calculations were performed with a plane-wave basis cutoff energy of 520 eV. The total energies were converged within $10^{-6}$ eV with a Monkhorst–Pack k-mesh[72] with 8000 k-points per reciprocal atom in the Brillouin zone. Spin–orbit coupling (SOC) was taken into account only in the band structure calculations.

## Supporting Information

Supporting Information is available from the Wiley Online Library or from the author.

## Acknowledgements

This work was supported by the U.S. Department of Energy, Office of Science and Office of Basic Energy Sciences under award number DE-SC0014520-0003. This work made use of the EPIC facility of Northwestern University's NUANCE Center, which has received support from the Soft and Hybrid Nanotechnology Experimental (SHyNE) Resource (NSF ECCS-1542205); the MRSEC program (NSF DMR-1720139) at the Materials Research Center; the International Institute for Nanotechnology (IIN); the Keck Foundation; the State of Illinois, through the IIN. This material is based upon work supported by the National Science Foundation Graduate Research Fellowship under Grant No. DGE-1324585. PYSA measurements were carried out with equipment acquired by ONR grant N00014-18-1-2102.

## Conflict of Interest

The authors declare no conflict of interest.

## Keywords

band structure engineering, grain boundary charge transport, low thermal conductivity, PbSe alloying, thermoelectric materials

Received: April 26, 2019
Revised: May 24, 2019
Published online: July 1, 2019

[1] D. Champier, *Energy Convers. Manage.* **2017**, *140*, 167.
[2] Y. Zhang, *ACS Energy Lett.* **2018**, *3*, 1523.
[3] F. J. DiSalvo, *Science* **1999**, *285*, 703.
[4] G. Tan, L.-D. Zhao, M. G. Kanatzidis, *Chem. Rev.* **2016**, *116*, 12123.
[5] J. R. Sootsman, D. Y. Chung, M. G. Kanatzidis, *Angew. Chem., Int. Ed.* **2009**, *48*, 8616.
[6] C. Wood, *Rep. Prog. Phys.* **1988**, *51*, 459.
[7] A. Mehdizadeh Dehkordi, M. Zebarjadi, J. He, T. M. Tritt, *Mater. Sci. Eng., R* **2015**, *97*, 1.
[8] Y. Pei, H. Wang, G. J. Snyder, *Adv. Mater.* **2012**, *24*, 6125.
[9] Y. Pei, X. Shi, A. LaLonde, H. Wang, L. Chen, G. J. Snyder, *Nature* **2011**, *473*, 66.
[10] M. G. Kanatzidis, *Chem. Mater.* **2010**, *22*, 648.
[11] L.-D. Zhao, V. P. Dravid, M. G. Kanatzidis, *Energy Environ. Sci.* **2014**, *7*, 251.
[12] J. He, M. G. Kanatzidis, V. P. Dravid, *Mater. Today* **2013**, *16*, 166.
[13] J. P. Heremans, V. Jovovic, E. S. Toberer, A. Saramat, K. Kurosaki, A. Charoenphakdee, S. Yamanaka, G. J. Snyder, *Science* **2008**, *321*, 554.
[14] K. Biswas, J. He, I. D. Blum, C.-I. Wu, T. P. Hogan, D. N. Seidman, V. P. Dravid, M. G. Kanatzidis, *Nature* **2012**, *489*, 414.
[15] G. Tan, F. Shi, S. Hao, L.-D. Zhao, H. Chi, X. Zhang, C. Uher, C. Wolverton, V. P. Dravid, M. G. Kanatzidis, *Nat. Commun.* **2016**, *7*, 12167.
[16] J. M. Hodges, S. Hao, J. A. Grovogui, X. Zhang, T. P. Bailey, X. Li, Z. Gan, Y.-Y. Hu, C. Uher, V. P. Dravid, C. Wolverton, M. G. Kanatzidis, *J. Am. Chem. Soc.* **2018**, *140*, 18115.
[17] H. Wang, Z. M. Gibbs, Y. Takagiwa, G. J. Snyder, *Energy Environ. Sci.* **2014**, *7*, 804.
[18] L.-D. Zhao, S. Hao, S.-H. Lo, C.-I. Wu, X. Zhou, Y. Lee, H. Li, K. Biswas, T. P. Hogan, C. Uher, C. Wolverton, V. P. Dravid, M. G. Kanatzidis, *J. Am. Chem. Soc.* **2013**, *135*, 7364.
[19] A. A. El-Sharkawy, A. M. Abou El-Azm, M. I. Kenawy, A. S. Hillal, H. M. Abu-Basha, *Int. J. Thermophys.* **1983**, *4*, 261.
[20] I. U. I. Ravich, B. A. Efimova, I. A. Smirnov, *Semiconducting Lead Chalcogenides*, Plenum Press, New York **1970**.
[21] Z.-Z. Luo, S. Hao, X. Zhang, X. S. Cai, G. Tan, T. P. Bailey, R. Ma, C. Uher, C. Wolverton, V. P. Dravid, Q. Yan, M. G. Kanatzidis, *Energy Environ. Sci.* **2018**, *11*, 3220.
[22] X. Qian, Y. Xiao, C. Chang, L. Zheng, L. Zhao, *Prog. Nat. Sci.: Mater. Int.* **2018**, *28*, 275.
[23] C.-F. Wu, T.-R. Wei, F.-H. Sun, J.-F. Li, *Adv. Sci.* **2017**, *4*, 1700199.
[24] Y. Lee, S.-H. Lo, C. Chen, H. Sun, D.-Y. Chung, T. C. Chasapis, C. Uher, V. P. Dravid, M. G. Kanatzidis, *Nat. Commun.* **2014**, *5*, 3640.
[25] L. You, Y. Liu, X. Li, P. Nan, B. Ge, Y. Jiang, P. Luo, S. Pan, Y. Pei, W. Zhang, G. J. Snyder, J. Yang, J. Zhang, J. Luo, *Energy Environ. Sci.* **2018**, *11*, 1848.
[26] Z. Chen, B. Ge, W. Li, S. Lin, J. Shen, Y. Chang, R. Hanus, G. J. Snyder, Y. Pei, *Nat. Commun.* **2017**, *8*, 13828.
[27] K. F. Hsu, S. Loo, F. Guo, W. Chen, J. S. Dyck, C. Uher, T. Hogan, E. K. Polychroniadis, M. G. Kanatzidis, *Science* **2004**, *303*, 818.
[28] P. F. P. Poudeu, J. D'Angelo, A. D. Downey, J. L. Short, T. P. Hogan, M. G. Kanatzidis, *Angew. Chem., Int. Ed.* **2006**, *45*, 3835.
[29] P. F. P. Poudeu, A. Guéguen, C.-I. Wu, T. Hogan, M. G. Kanatzidis, *Chem. Mater.* **2010**, *22*, 1046.
[30] T. J. Slade, J. A. Grovogui, S. Hao, T. P. Bailey, R. Ma, X. Hua, A. Guéguen, C. Uher, C. Wolverton, V. P. Dravid, M. G. Kanatzidis, *J. Am. Chem. Soc.* **2018**, *140*, 7021.
[31] J. Mao, J. Shuai, S. Song, Y. Wu, R. Dally, J. Zhou, Z. Liu, J. Sun, Q. Zhang, C. dela Cruz, S. Wilson, Y. Pei, D. J. Singh, G. Chen, C.-W. Chu, Z. Ren, *Proc. Natl. Acad. Sci. USA* **2017**, *114*, 10548.
[32] J. Zhang, L. Song, S. H. Pedersen, H. Yin, L. T. Hung, B. B. Iversen, *Nat. Commun.* **2017**, *8*, 13901.

[33] J. J. Kuo, S. D. Kang, K. Imasato, H. Tamaki, S. Ohno, T. Kanno, G. J. Snyder, *Energy Environ. Sci.* **2018**, *11*, 429.
[34] J. He, L.-D. Zhao, J.-C. Zheng, J. W. Doak, H. Wu, H.-Q. Wang, Y. Lee, C. Wolverton, M. G. Kanatzidis, V. P. Dravid, *J. Am. Chem. Soc.* **2013**, *135*, 4624.
[35] C. B. Lioutas, N. Frangis, I. Todorov, D. Y. Chung, M. G. Kanatzidis, *Chem. Mater.* **2010**, *22*, 5630.
[36] S. V. Barabash, V. Ozolins, C. Wolverton, *Phys. Rev. Lett.* **2008**, *101*, 155704.
[37] X. Hua, V. I. Hedge, C. Wolverton, *In preparation*.
[38] N. Chen, F. Gascoin, G. J. Snyder, E. Müller, G. Karpinski, C. Stiewe, *Applied Physical Letters* **2005**, *87*, 171903.
[39] B. Abeles, *Phys. Rev.* **1963**, *131*, 1906.
[40] W. G. Zeier, A. Zevalkink, Z. M. Gibbs, G. Hautier, M. G. Kanatzidis, G. J. Snyder, *Angew. Chem., Int. Ed.* **2016**, *55*, 6826.
[41] H. Wang, Y. Pei, A. D. LaLonde, G. J. Snyder, *Proc. Natl. Acad. Sci. USA* **2012**, *109*, 9705.
[42] Y. Pei, A. D. LaLonde, H. Wang, G. J. Snyder, *Energy Environ. Sci.* **2012**, *5*, 7963.
[43] T. C. Chasapis, Y. Lee, E. Hatzikraniotis, K. M. Paraskevopoulos, H. Chi, C. Uher, M. G. Kanatzidis, *Phys. Rev. B* **2015**, *91*, 085207.
[44] Y. Pei, A. D. LaLonde, N. A. Heinz, X. Shi, S. Iwanaga, H. Wang, L. Chen, G. J. Snyder, *Adv. Mater.* **2011**, *23*, 5674.
[45] R. S. Allgaier, B. B. Houston Jr., *J. Appl. Phys.* **1966**, *37*, 302.
[46] L. D. Zhao, H. J. Wu, S. Q. Hao, C. I. Wu, X. Y. Zhou, K. Biswas, J. Q. He, T. P. Hogan, C. Uher, C. Wolverton, V. P. Dravid, M. G. Kanatzidis, *Energy Environ. Sci.* **2013**, *6*, 3346.
[47] R. S. Allgaier, *J. Appl. Phys.* **1965**, *36*, 2429.
[48] R. S. Allgaier, *J. Appl. Phys.* **1961**, *32*, 2185.
[49] J. R. Harwell, T. K. Baikie, I. D. Baikie, J. L. Payne, C. Ni, J. T. S. Irvine, G. A. Turnbull, I. D. W. Samuel, *Phys. Chem. Chem. Phys.* **2016**, *18*, 19738.
[50] I. Spanopoulos, I. Hadar, W. Ke, Q. Tu, M. Chen, H. Tsai, Y. He, G. Shekhawat, V. P. Dravid, M. R. Wasielewski, A. D. Mohite, C. C. Stoumpos, M. G. Kanatzidis, *J. Am. Chem. Soc.* **2019**, *141*, 5518.
[51] I. D. Baikie, A. Grain, J. Sutherland, J. Law, *Phys. Status Solidi C* **2015**, *12*, 259.
[52] H. Wang, X. Cao, Y. Takagiwa, G. J. Snyder, *Mater. Horiz.* **2015**, *2*, 323.
[53] H. S. Kim, W. Liu, Z. Ren, *Energy Environ. Sci.* **2017**, *10*, 69.
[54] P. Jood, M. Ohta, A. Yamamoto, M. G. Kanatzidis, *Joule* **2018**, *2*, 1339.
[55] X. Hu, P. Jood, M. Ohta, M. Kunii, K. Nagase, H. Nishiate, M. G. Kanatzidis, A. Yamamoto, *Energy Environ. Sci.* **2016**, *9*, 517.
[56] G. J. Snyder, A. H. Snyder, *Energy Environ. Sci.* **2017**, *10*, 2280.
[57] G. Tan, S. Hao, S. Cai, T. P. Bailey, Z. Luo, I. Hadar, C. Uher, V. P. Dravid, C. Wolverton, M. G. Kanatzidis, *J. Am. Chem. Soc.* **2019**, *141*, 4480.
[58] K. F. Cai, X. R. He, M. Avdeev, D. H. Yu, J. L. Cui, H. Li, *J. Solid State Chem.* **2008**, *181*, 1434.
[59] L. Pan, S. Mitra, L.-D. Zhao, Y. Shen, Y. Wang, C. Felser, D. Berardan, *Adv. Funct. Mater.* **2016**, *26*, 5149.
[60] S. Wang, S. Hui, K. Peng, T. P. Bailey, X. Zhou, X. Tang, C. Uher, *J. Mater. Chem. C* **2017**, *5*, 10191.
[61] J. Y. W. Seto, *J. Appl. Phys.* **1975**, *46*, 5247.
[62] J. W. Orton, M. J. Powell, *Rep. Prog. Phys.* **1980**, *43*, 1263.
[63] K. A. Borup, J. de Boor, H. Wang, F. Drymiotis, F. Gascoin, X. Shi, L. Chen, M. I. Fedorov, E. Muller, B. B. Iversen, G. J. Snyder, *Energy Environ. Sci.* **2015**, *8*, 423.
[64] R. Blachnik, R. Igel, *Z. Naturforsch., B* **1974**, *29*, 625.
[65] P. Hohenberg, W. Kohn, *Phys. Rev.* **1964**, *136*, B864.
[66] W. Kohn, L. J. Sham, *Phys. Rev.* **1965**, *140*, A1133.
[67] G. Kresse, J. Hafner, *Phys. Rev. B* **1994**, *49*, 14251.
[68] G. Kresse, J. Hafner, *Phys. Rev. B* **1993**, *47*, 558.
[69] G. Kresse, J. Furthmüller, *Phys. Rev. B* **1996**, *54*, 11169.
[70] P. E. Blöchl, *Phys. Rev. B* **1994**, *50*, 17953.
[71] J. P. Perdew, K. Burke, M. Ernzerhof, *Phys. Rev. Lett.* **1996**, *77*, 3865.
[72] H. J. Monkhorst, J. D. Pack, *Phys. Rev. B* **1976**, *13*, 5188.

 